RESEARCH ARTICLE

WILEY

Deep learning-guided joint attenuation and scatter correction in multitracer neuroimaging studies

Hossein Arabi[1] | Karin Bortolin[1] | Nathalie Ginovart[2,3] | Valentina Garibotto[1,4] | Habib Zaidi[1,4,5,6]

[1]Division of Nuclear Medicine and Molecular Imaging, Department of Medical Imaging, Geneva University Hospital, Geneva, Switzerland

[2]Department of Psychiatry, Geneva University, Geneva, Switzerland

[3]Department of Basic Neurosciences, Geneva University, Geneva, Switzerland

[4]Geneva Neuroscience Center, Geneva University, Geneva, Switzerland

[5]Department of Nuclear Medicine and Molecular Imaging, University of Groningen, University Medical Center Groningen, Groningen, Netherlands

[6]Department of Nuclear Medicine, University of Southern Denmark, Odense, Denmark

Correspondence
Habib Zaidi, Division of Nuclear Medicine and Molecular Imaging, Geneva University Hospital, Geneva CH-1211, Switzerland.
Email: habib.zaidi@hcuge.ch

Abstract

PET attenuation correction (AC) on systems lacking CT/transmission scanning, such as dedicated brain PET scanners and hybrid PET/MRI, is challenging. Direct AC in image-space, wherein PET images corrected for attenuation and scatter are synthesized from nonattenuation corrected PET (PET-nonAC) images in an end-to-end fashion using deep learning approaches (DLAC) is evaluated for various radiotracers used in molecular neuroimaging studies. One hundred eighty brain PET scans acquired using ^{18}F-FDG, ^{18}F-DOPA, ^{18}F-Flortaucipir (targeting tau pathology), and ^{18}F-Flutemetamol (targeting amyloid pathology) radiotracers (40 + 5, training/validation + external test, subjects for each radiotracer) were included. The PET data were reconstructed using CT-based AC (CTAC) to generate reference PET-CTAC and without AC to produce PET-nonAC images. A deep convolutional neural network was trained to generate PET attenuation corrected images (PET-DLAC) from PET-nonAC. The quantitative accuracy of this approach was investigated separately for each radiotracer considering the values obtained from PET-CTAC images as reference. A segmented AC map (PET-SegAC) containing soft-tissue and background air was also included in the evaluation. Quantitative analysis of PET images demonstrated superior performance of the DLAC approach compared to SegAC technique for all tracers. Despite the relatively low quantitative bias observed when using the DLAC approach, this approach appears vulnerable to outliers, resulting in noticeable local pseudo uptake and false cold regions. Direct AC in image-space using deep learning demonstrated quantitatively acceptable performance with less than 9% absolute SUV bias for the four different investigated neuroimaging radiotracers. However, this approach is vulnerable to outliers which result in large local quantitative bias.

KEYWORDS
attenuation correction, deep learning, neuroimaging tracers, PET, quantification

1 | INTRODUCTION

Positron emission tomography (PET) plays a key role in noninvasive assessment of brain function and understating biochemical dynamics. In particular, PET imaging is utilized for the diagnosis of neurodegenerative diseases, such as dementia of Alzheimer type and Parkinson disease. In clinical practice, ^{18}F-fluorodeoxyglucose (FDG) is the most commonly used radiotracer in brain imaging. However, brain imaging using more specific radiotracers, such as ^{18}F-labeled amino acid L-tyrosine (^{18}F-FET), ^{18}F-Flutemetamol (Vizamyl™), ^{18}F–fluoro-dihydroxyphenylalanine (^{18}F-DOPA), and ^{18}F-Flortaucipir agents is an active and growing area.

[18]F-Flutemetamol diagnostic agent is used in adult patients to estimate the density of beta-amyloid neurotic plaque to investigate Alzheimer's disease pathology in subjects with cognitive decline (Chiotis et al., 2017; Hammers et al., 2017). PET scanning using ^{18}F-DOPA enables measuring the uptake of dopamine precursors in Parkinson disease, which has been demonstrated to reflect the monoaminergic degenerative process (Pavese & Brooks, 2009). ^{18}F-Flortaucipir is performed to investigate tau pathology, mainly in Alzheimer's disease, and with lower affinity in other neurodegenerative disorders, such as progressive supranuclrear palsy and corticobasal degeneration (Leuzy et al., 2019; Noirot et al., 2018).

PET neuroimaging has witnessed steady growth over the years with the introduction of novel specific radiotracers, which triggered the development of dedicated brain PET systems, allowing for significantly higher spatial resolution compared to conventional whole-body PET scanners (Melroy et al., 2017; Tashima et al., 2016; Zaidi & Montandon, 2006). Despite the expanding demand for functional brain imaging, dedicated brain PET scanners face the challenge of attenuation and scatter correction since they are not always equipped with concurrent computed tomography (CT) scanning that readily provides information about attenuating medium. Likewise, PET scanners coupled with magnetic resonance imaging (MRI) require accurate and robust attenuation correction (AC) since MR intensity in structural images is not correlated with the attenuation coefficients of biologic tissues (Mehranian, Arabi, & Zaidi, 2016b).

Scatter and ACs are critical for both reliable qualitative interpretation and accurate quantification of PET images (Zaidi & Koral, 2004; Zaidi, Montandon, & Meikle, 2007). In the absence of transmission imaging to derive attenuation maps, current strategies used to generate AC maps, either with or without the use of structural MR images, could be categorized into three generic approaches (Mehranian et al., 2016b): (a) Bulk segmentation-based methods attempt to discriminate the different tissue classes from MRI, including the use of dedicated MR sequences to depict bony structures as a separate tissue class (Keereman et al., 2010), to assign predefined tissue-specific attenuation coefficients (Arabi et al., 2015; Martinez-Moller et al., 2009); (b) Atlas-based and machine learning methods rely on coregistered pairs of MR/CT images to generate substitute CT image using a mapping function between MR and CT images (Arabi, Koutsouvelis, Rouzaud, Miralbell, & Zaidi, 2016; Arabi & Zaidi, 2016b; Wollenweber et al., 2013) or a nonlinear training process to predict synthetic CT from MR images (Arabi & Zaidi, 2016a); (c) Joint activity/attenuation map estimation from PET emission data taking advantage of the availability of time-of-flight (TOF) information (Defrise, Rezaei, & Nuyts, 2012). Exploitation of MRI information has been shown to enhance the accuracy of the joint activity/attenuation reconstruction (Mehranian, Arabi, & Zaidi, 2016a; Mehranian, Zaidi, & Reader, 2017). A multicentric comparison of 11 MRI-guided AC techniques in brain PET imaging demonstrated the superior performance of methods relying on atlas prior information or dedicated MR sequences capable of bone detection to segmentation-based and joint activity/attenuation reconstruction approaches (Ladefoged et al., 2017). Yet, this study did not include any machine learning-guided approaches, such as random forest (Huynh et al., 2016) convolutional neural network (Han, 2017; Liu, Jang, Kijowski, Bradshaw, & McMillan, 2017) and generative adversarial network techniques (Arabi, Zeng, Zheng, & Zaidi, 2019), which have shown promising performance in synthetic CT generation directly from MR images provided a sufficient MRI/CT pairs dataset is available for training.

Recently, deep learning algorithms have been widely utilized in various medical image analysis problems owing to the promising results achieved in image segmentation, regression, denoising, and radiomics analysis (Arabi et al., 2018; Litjens et al., 2017). Most of the studies addressing PET AC focused on the generation of synthetic CT images from a single or multiple MR sequences (Emami, Dong, Nejad-Davarani, & Glide-Hurst, 2018; Han, 2017; Liu et al., 2018). The primary objective of these studies is to improve MRI-guided CT synthesis in the head (Arabi et al., 2019; Dinkla et al., 2018) and pelvis (Leynes et al., 2018) regions for use in PET/MR quantitative imaging or MRI-only treatment planning.

In addition to MRI-guided CT synthesis, owing to the outstanding versatility of deep learning approaches, attenuation, and scatter correction directly in the image domain without using the anatomical information has been reported (Shiri et al., 2019; Yang, Park, Gullberg, & Seo, 2019). In this regard, a deep convolutional neural network was trained to learn the end-to-end conversion between non-attenuation corrected (PET-nonAC) and CT-based attenuation and scatter corrected PET images (PET-CTAC) in image-space. So far, this approach has been evaluated only on brain ^{18}F-FDG PET images (Yang et al., 2019). To the best of our knowledge this approach has not been evaluated for other clinically relevant radiotracers used in neuroimaging, such as ^{18}F-Flortaucipir, ^{18}F-DOPA, and ^{18}F-Flutemetamol.

The aim of this work is to carry out a comprehensive assessment of direct attenuation and scatter correction in image-space using deep learning algorithms for various PET neuroimaging radiotracers. Even though other MRI-guided AC approaches (e.g., atlas-based) achieved uptake bias of less than 5% (Ladefoged et al., 2017), direct attenuation and scatter correction in image-space is of special interest as it does not require anatomical imaging. To this end, 180 PET/CT brain scans (160 in a fivefold cross-validation and 20 as external test dataset) using four different neuroimaging radiotracers (forty patients for each radiotracer), namely ^{18}F-FDG, ^{18}F-DOPA, ^{18}F-Flutemetamol, and ^{18}F-Flortaucipir, were used to evaluate the performance of the approach. PET-CTAC images were considered as reference for evaluation, whereas a segmentation-based attenuation map (SegAC—containing background air and soft-tissue) derived from a two-class segmentation of the

PET-nonAC was included in the evaluation as a proxy for segmentation-based AC used on commercial PET/MR scanners (Zaidi et al., 2011). In addition to quantitative assessment of this approach for different PET neuroimaging radiotracers, we particularly focused on outliers and large bias which might occur when using deep learning algorithms, in general, and when direct attenuation and scatter correction is performed in image-space, in particular.

2 | MATERIALS AND METHODS

2.1 | PET/CT data acquisition

Time-of-flight (TOF) brain PET/CT scans of 180 patients were retrospectively employed for the quantitative evaluation of the attenuation and scatter correction technique in the image domain using a deep learning algorithm. The evaluation was performed separately for four different PET radiotracers, namely, ^{18}F-FDG, ^{18}F-DOPA, ^{18}F-Flutemetamol, and ^{18}F-Flortaucipir (45 patients for each radiotracer). The study protocol was approved by the ethics committee of Geneva University Hospitals and all patients gave informed consent. All patients underwent a PET/CT on the Biograph mCT scanner (Siemens Healthcare, Erlangen, Germany). A low-dose CT scan was performed prior to radiotracer injection for PET AC using the following parameters: 20 mAs, 0.3 s/rotation, 120 kVp, and a voxel size of $0.9 \times 0.9 \times 2.5$ mm^3. For ^{18}F-FDG scanning protocol, PET data acquisition started 32 ± 6 min after injection of 208 ± 14 MBq ^{18}F-FDG in a single bed position for 20 min. PET scans using the ^{18}F-Flortaucipir agent lasted 30 min after injection of 205 ± 10 MBq. The acquisition stared 76 ± 8 min after injection. ^{18}F-Flutemetamol PET scans started 91 ± 6 min after injection of 199 ± 11 MBq for an acquisition time of 20 min. ^{18}F-DOPA PET data acquisition started at the time of injection of 185 ± 12 MBq for a total acquisition time of 90 min. Patient's demographic and clinical characteristics pertinent to each radiotracer are summarized in Table 1.

Siemens e7 tool was used to reconstruct the PET raw data using an ordinary Poisson ordered subsets-expectation maximization with TOF information (TOF OP-OSEM) adopting default parameters used in the clinic (5 iteration, 21 subsets). Scatter correction was performed using the single scatter simulation (SSS) algorithm with tail fitting for scaling. PET image reconstruction was repeated without attenuation and scatter correction to generate PET-nonAC images. PET images were reconstructed in a $200 \times 200 \times 109$ matrix (voxel size of $2 \times 2 \times 2$ mm) followed by Gaussian filtering with 2 mm FWHM.

In addition, 20 patients (five subjects for each radiotracer) were later added as external test dataset to further assess the generalizability of this approach.

2.2 | Deep learning algorithm

The Niftynet, an open-source convolutional neural network pipeline, was employed to implement attenuation and scatter correction in the image-space. The Niftynet infrastructure provides a modular deep-learning platform for common medical imaging applications and computer-assisted intervention (Gibson et al., 2018). The Niftynet platform, built on TensorFlow (version 1.12) in Python (version 3.6), enables researchers to rapidly implement deep learning solutions based on state-of-the-art convolutional neural network architectures. The application of deep learning-based image regression was used to predict PET attenuation and scatter corrected (PET-DLAC) from PET-nonAC images in an end-to-end fashion. To this end, a neural network was trained using the net_regress application. This application calls on a state-of-the-art compact so-called highresnet convolutional neural network, developed originally for volumetric image segmentation (Li et al., 2017). Since this residual network takes features at multiple levels (scales) into account, it maintains the spatial resolution of the input images throughout the network, which enables direct fusion of features from different levels or scales. Our preliminary experiments showed the superior performance of this network to the well-established U-net and encoder–decoder structures and its slightly better performance over generative adversarial networks.

This network consists of 20 convolutional layers wherein in the first seven layers, a convolution kernel of $3 \times 3 \times 3$-voxel is applied. The first seven layers are designed to encode low-level features (such as edges and corners) from the input image. In the subsequent seven and six convolutional layers, the kernel is dilated by a factor of two and four, respectively, to capture medium and high-level features. Every two convolutional layers are linked by a residual connection. Convolutional layers within the residual blocks are connected to a batch normalization layer and an element-wise rectified linear unit (ReLU) Figure S1.

2.2.1 | Implementation details

For each of the four neuroimaging tracers, pairs of PET-CTAC and PET-nonAC images were utilized as input/output for the training and

TABLE 1 Clinical characteristics and patient demographics of the clinical brain PET studies

	^{18}F-Flortaucipir	^{18}F-FDG	^{18}F-Flutemetamol	^{18}F-DOPA
Age (mean, range)	66.5 (58–78)	62.2 (51–81)	63.1 (45–77)	25.4 (20–40)
Gender	19F/26M	27F/18M	23F/22M	18F/27M
Indication/diagnosis	Cognitive symptoms of possible neurodegenerative etiology			11 healthy controls 25 patients with a cannabis use disorder 8 patients with an internet gaming disorder 1 patient with neuroendocrine tumor

evaluation of the direct attenuation and scatter correction technique. In the first step, the voxel values of PET-CTAC and PET-nonAC images were converted to standard uptake value (SUV) scale. Thereafter, the intensities of PET images were scaled down using a fixed normalization factor separately for each dataset to reduce the dynamic range of the image values. For ^{18}F-FDG radiotracer, PET-CTAC and PET-nonAC images were normalized by factors of 10 and 2.1, respectively. ^{18}F-DOPA PET-CTAC and PET-nonAC were normalized by factors 3 and 1, respectively. Normalization factors of 1.5 and

0.3 were utilized for ^{18}F-Flutemetamol PET-CTAC and PET-nonAC images, respectively. ^{18}F-Flortaucipir PET-CTAC and PET-nonAC images were normalized by factors of 1.8 and 0.7, respectively. Thereafter, PET images were cropped to $128 \times 128 \times 105$ voxels to cutoff background air as much as possible in an effort to reduce the computational burden.

The highresnet model, implemented in the Niftynet infrastructure, was trained using a spatial window = 128×128, learning rate = 0.002, optimizer = Adam, loss function = L2norm, decay = 0.0001, batch

TABLE 2 Quantitative accuracy of SUV estimation using DLAC and SegAC approaches using CTAC as reference for assessment together with RMSE, SSIM and PSNR calculated over 40 patients within the entire head region for ^{18}F-Flortaucipir, ^{18}F-Flutemetamol, ^{18}F-FDG, and ^{18}F-DOPA brain PET studies

[18]F-Flortaucipir	ME (SUV)	MAE (SUV)	RE (%)	RMSE (SUV)	PSNR (dB)	SSIM
PET-DLAC	−0.02 ± 0.01	0.08 ± 0.02	3.6 ± 4.9	0.09 ± 0.02	34.7 ± 3.8	0.96 ± 0.02
PET-SegAC	−0.30 ± 0.06	0.41 ± 0.08	−6.2 ± 4.0	0.45 ± 0.08	31.9 ± 3.7	0.92 ± 0.02
[18]F-Flutemetamol						
PET-DLAC	−0.01 ± 0.01	0.05 ± 0.01	2.1 ± 3.3	0.07 ± 0.02	36.0 ± 3.6	0.97 ± 0.02
PET-SegAC	−0.26 ± 0.05	0.36 ± 0.07	−6.0 ± 3.9	0.42 ± 0.07	32.7 ± 3.5	0.93 ± 0.02
^{18}F-FDG						
PET-DLAC	0.12 ± 0.75	0.18 ± 0.46	3.1 ± 6.9	0.20 ± 0.38	34.2 ± 3.3	0.94 ± 0.02
PET-SegAC	−0.40 ± 0.35	0.42 ± 0.30	−6.4 ± 5.8	0.51 ± 0.29	32.1 ± 3.2	0.90 ± 0.03
^{18}F-DOPA						
PET-DLAC	−0.11 ± 0.68	0.17 ± 0.39	3.9 ± 6.9	0.20 ± 0.37	34.9 ± 3.1	0.94 ± 0.02
PET-SegAC	−0.37 ± 0.32	0.40 ± 0.28	−7.1 ± 6.1	0.49 ± 0.27	32.3 ± 3.0	0.91 ± 0.03

TABLE 3 PET quantification bias calculated within soft-tissue, air cavities and bone regions for ^{18}F-Flortaucipir, ^{18}F-Flutemetamol, ^{18}F-FDG, and ^{18}F-DOPA PET images for DLAC and SegAC AC approaches

[18]F-Flortaucipir				^{18}F-Flutemetamol		
Soft-tissue	ME (SUV)	MAE (SUV)	RE (%)	ME (SUV)	MAE (SUV)	RE (%)
PET-DLAC	−0.02 ± 0.01	0.05 ± 0.02	2.0 ± 4.2	−0.01 ± 0.01	0.07 ± 0.02	2.2 ± 3.7
PET-SegAC	0.08 ± 0.05	0.16 ± 0.07	3.3 ± 3.9	0.07 ± 0.04	0.15 ± 0.06	3.5 ± 3.9
Bone						
PET-DLAC	−0.03 ± 0.02	0.06 ± 0.03	−1.9 ± 6.2	−0.03 ± 0.03	0.07 ± 0.07	−2.0 ± 6.4
PET-SegAC	−0.18 ± 0.05	0.20 ± 0.05	−7.0 ± 6.7	−0.17 ± 0.06	0.22 ± 0.06	−7.1 ± 6.8
Air cavity						
PET-DLAC	0.02 ± 0.11	0.03 ± 0.10	4.0 ± 6.5	0.03 ± 0.12	0.04 ± 0.11	4.2 ± 6.6
PET-SegAC	0.11 ± 0.21	0.12 ± 0.19	24.2 ± 8.4	0.13 ± 0.23	0.15 ± 0.19	26.3 ± 9.0
^{18}F-FDG				**[18]F-DOPA**		
Soft-tissue	ME (SUV)	MAE (SUV)	RE (%)	ME (SUV)	MAE (SUV)	RE (%)
PET-DLAC	0.11 ± 0.69	0.17 ± 0.45	1.9 ± 5.7	−0.09 ± 0.61	0.15 ± 0.39	−2.8 ± 5.9
PET-SegAC	−0.39 ± 0.33	0.41 ± 0.30	−4.1 ± 6.7	−0.31 ± 0.29	0.39 ± 0.27	−4.9 ± 6.0
Bone						
PET-DLAC	0.08 ± 0.52	0.10 ± 0.47	1.8 ± 7.1	−0.07 ± 0.48	0.09 ± 0.42	−1.9 ± 6.4
PET-SegAC	−0.29 ± 0.26	0.30 ± 0.26	−14.0 ± 6.6	−0.26 ± 0.25	0.29 ± 0.24	−13.1 ± 5.8
Air cavity						
PET-DLAC	0.02 ± 0.12	0.03 ± 0.11	4.2 ± 6.8	0.02 ± 0.10	0.03 ± 0.11	4.4 ± 6.5
PET-SegAC	0.12 ± 0.21	0.13 ± 0.20	37.2 ± 8.9	0.11 ± 0.20	0.13 ± 0.19	38.4 ± 9.0

size = 120, sample per volume = 1 and queue length = 480. It should be noted that training was performed in two-dimensional (2D) and three-dimensional (3D) modes using a spatial window = $128 \times 128 \times 32$ for the 3D mode. However, visual inspection and quantitative analysis revealed slightly better performance of 2D training. For each radiotracer dataset, considering a batch size of 120, the training of the model took about ~22 hr using an Intel(R) Xeon 2.30 GHz 7i CPU and 64 GB RAM computer. The loss function of the model reached a plateau after 8 epochs. The synthesis of PET images, in the inference step, took 5 s for each patient (whole brain study). The training of the model was repeated five times for each of radiotracer following a five-fold cross-validation scheme (32 images for training and 8 images for test datasets). No pretrained model or transfer learning were used for the training of these models owing to the fact that transfer learning (for instance using the trained model by the ^{18}F-FDG datasets to initiate the training of the ^{18}F-DOPA datasets) did not improve the outcomes of the models. Overall, 20 independent models were trained and tested. As such, the quantitative analysis was performed on all 40 patients as well as the five external subjects for each neuroimaging radiotracer. For the training of the models, single-slice (in 2D training mode) and batches of 32 slices (in 3D training mode) samples were taken randomly from the 3D input subjects. These samples were taken uniformly from the whole field-of-view of the brain PET scan. Since no significant improvement was observed, data augmentation was not implemented in the training process.

2.3 | Quantitative evaluation

The performance of direct attenuation and scatter correction was evaluated against CT-based AC serving as reference. Moreover, as a bottom line of clinically tolerable errors, a segmented attenuation map (SegAC), as a proxy for the commercially implemented MRI-guided AC, was included in the evaluation. SegAC attenuation maps were derived from 2-class segmentation of TOF reconstructed PET-nonAC images. The contour of the head was delineated using thresholding followed by the assignment of attenuation coefficients of 0.1 cm^{-1} ($\approx$ 0 HU) and 0.0 cm^{-1} ($\approx$ −1,000 HU) to voxels located inside and outside the head contour, respectively.

Considering PET-CTAC as reference, difference SUV images and bias maps were calculated separately within different tissue types, namely, bone, soft-tissue, and air cavities, for each of four the PET neuroimaging radiotracers. To this end, the following intensity threshold levels were used to segment bone (>160 HU), air cavities (< −400 HU within the head contour), and soft-tissue (> −400 and <160 HU) from CT images. The mean error (ME), absolute mean error (MAE), root mean square (RMSE) error, and SUV bias (relative error [RE(%)]) were calculated between reference PET-CTAC and PET-DLAC and PET-SegAC images using Equations (1)–(4), respectively.

$$ME = \frac{1}{v}\sum_{i=1}^{v}(PET_{test}(i) - PET_{ref}(i)) \tag{1}$$

$$MAE = \frac{1}{v}\sum_{i=1}^{v}|PET_{test}(i) - PET_{ref}(i)| \tag{2}$$

$$RMSE = \sqrt{\frac{1}{v}\sum_{i=1}^{v}(PET_{test}(i) - PET_{ref}(i))^2} \tag{3}$$

$$RE(\%) = \frac{1}{v}\sum_{i=1}^{v}\left(\frac{(PET_{test})_i - (PET_{ref})_i}{(PET_{ref})_i}\right) \times 100\% \tag{4}$$

where PET_{test} stands for PET images attenuation corrected using either the deep learning-based or SegAC technique. i and v variables indicate the voxel index and the total number of voxels, respectively.

Moreover, peak signal-to-noise ratio (PSNR) and structural similarity index (SSIM) metrics were computed to assess the similarity and accuracy of the generated PET images using Equations (5) and (6), respectively.

FIGURE 1 Comparison of PET images corrected for attenuation using CT-based, SegAC and DLAC approaches along with the reference CT image for the four different radiotracers. Difference SUV error maps are also shown for DLAC and SegAC approaches

$$PSNR(dB) = 10\log_{10}\left(\frac{Mv^2}{MSE}\right) \qquad (5)$$

$$SSIM = \frac{(2Mn_{ref}Mn_{test} + K_1)(2\delta_{ref,test} + K_2)}{\left(Mn_{ref}^2 + Mn_{test}^2 + K_1\right)\left(\delta_{ref}^2 + \delta_{test}^2 + K_2\right)} \qquad (6)$$

In Equation (5), Mv indicates the maximum intensity value of PET_{ref} or PET_{test} whereas MSE stands for the mean squared error. In Equation (6), Mn_{ref} and Mn_{test} represent the mean value of PET_{ref} and PET_{test} images, respectively. δ_{ref} and δ_{test} are the variances of PET_{ref} and PET_{test} images where their covariance is denoted $\delta_{ref,test}$. To avoid a division by a very small value, K_1 and K_2 constant parameters ($K_1 = 0.01$ and $K_2 = 0.02$) were inserted in Equation (6).

The abovementioned quantitative metrics were also calculated for the 20 subjects belonging to the external test dataset to investigate the potential performance discrepancies between the different training/validation folds as well as repeatability of this approach.

In addition, a joint histogram analysis was performed to display the voxel-wise distribution of radiotracer activity correlation between PET-DLAC/PET-SegAC and reference PET-CTAC for the different PET neuroimaging radiotracers.

For ^{18}F-FDG PET images, the quantitative evaluation of activity concentration was performed in 63 brain regions. To this end, the Hermes BRASS analysis tool (Hermes Medical Solutions AB, Sweden) was employed to define 63 brain regions on PET images that were used to calculate the relative mean error (RE(%)) and absolute mean error (ARE(%)) using Equations (7) and (8), respectively. Similarly, ^{18}F-Flortaucipir and ^{18}F-Flutemetamol PET images were spatially normalized to the Montreal Neurological Institute (MNI) reference space (Evans et al., 1993) using in-house developed tracer-dependent templates. Briefly, these templates were obtained by averaging PET images of the 40 subjects included in this study following normalization in MNI space by deriving the deformation maps from the individual MRI. Mean and absolute mean relative errors were calculated for 70 brain regions using Equations (7) and (8), respectively. The MNI template provides 136 distinct brain regions, but the left and right regions were merged in this work, thus reducing the total number of brain regions to 70. ^{18}F-DOPA PET images were also spatially normalized to MNI reference space using a publicly available ^{18}F-DOPA-PET

FIGURE 2 Mean absolute relative bias (%) and mean bias (%) of tracer uptake of PET-DLAC and PET-SegAC with respect to reference PET-CTAC for ^{18}F-Flortaucipir calculated for 70 brain regions

template (Gómez, Huertas, Ramírez, & Solís, 2018) to calculate relative mean and absolute mean errors in seven brain regions including posterior, frontal, cerebellum, right and left caudate, right and left putamen.

$$RE_{region}(\%) = \frac{(PET_{test})_{region} - (PET_{ref})_{region}}{(PET_{ref})_{region}} \times 100\% \qquad (7)$$

$$ARE_{region}(\%) = \left| \frac{(PET_{test})_{region} - (PET_{ref})_{region}}{(PET_{ref})_{region}} \right| \times 100\% \qquad (8)$$

In addition to quantitative analysis using the above metrics, the 180 PET-DLAC images were visually inspected to spot any pseudo uptakes, gross errors, and image artifacts. Special attention was paid to this task as deep learning algorithms, in general, and attenuation and scatter correction in image-space, in particular, are prone to unpredictable errors. Image artifacts and gross errors observed across the 180 patients were separately reported.

Paired t-test analysis was employed to prove statistical significance of the differences between the calculated metrics where a p-value less than .05 was considered statistically significant.

3 | RESULTS

For the sake of standardization, the tracer uptake in neuroimaging studies involving ^{18}F-Flortaucipir, ^{18}F-Flutemetamol, and ^{18}F-DOPA is usually reported in terms of SUV ratio (SUVR) obtained from normalizing to mean tracer uptake in the cerebellum or pons as these regions are commonly not affected until late during disease progression (Vemuri et al., 2017). In the present work, the accuracy of the different AC approaches was investigated by comparing the absolute SUVs since normalization to a reference region (SUVR) tends to undermine the assessment by hiding the actual underestimation/overestimation of tracer uptake. The evaluation of the different AC methods using the SUVR metric would complicate the interpretation of the results (e.g., overestimation in the target region and underestimation in the reference region would be confounded) and might lead to skewed conclusions as depicted in Figure S2. The SUV profile obtained from PET-SegAC image exhibits noticeable underestimation of tracer uptake. Yet, after normalization to the mean SUV in the cerebellum (which was similarly underestimated), the SUVR profile drawn on PET-SegAC agrees closely with PET-CTAC.
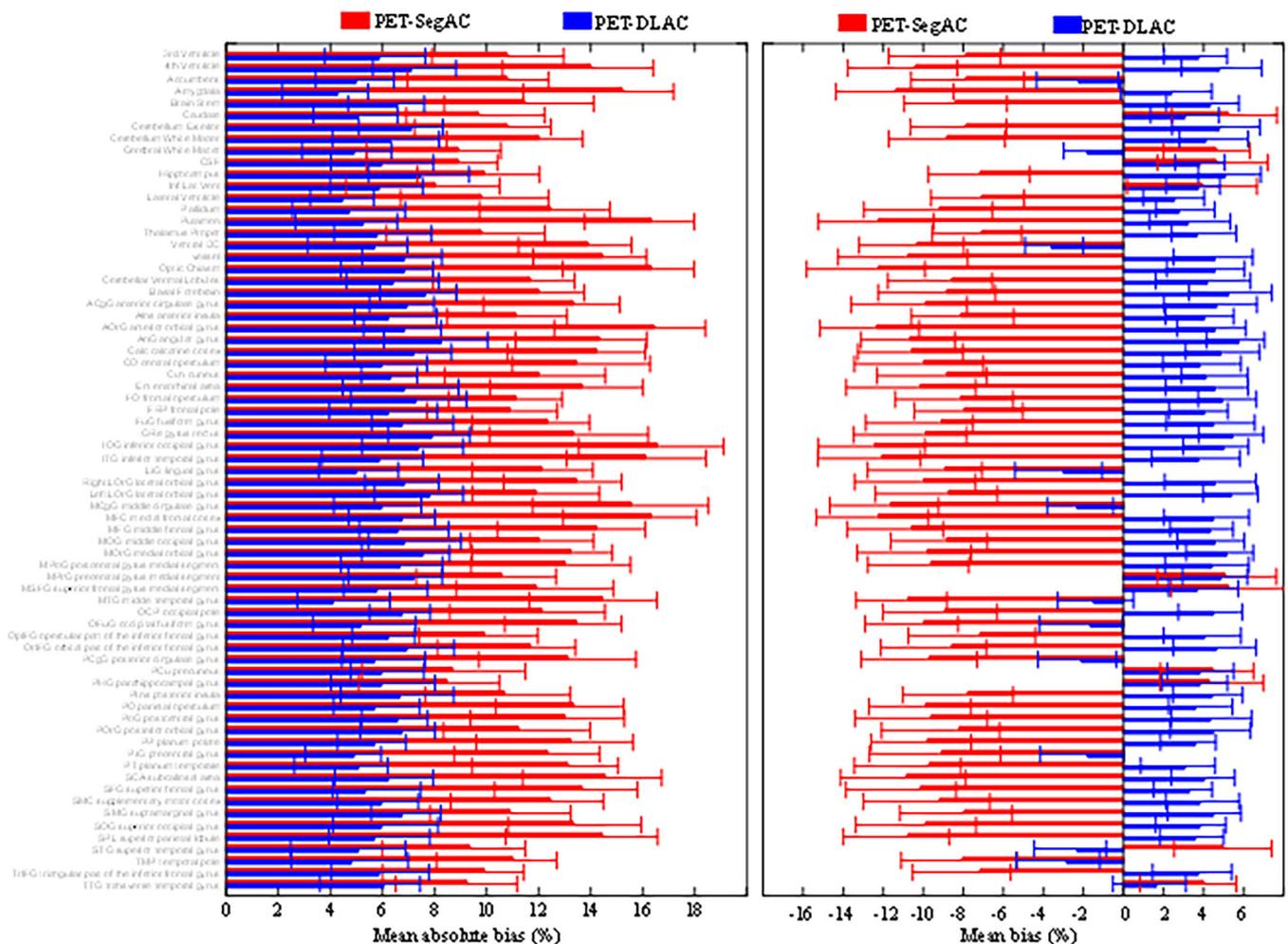
FIGURE 3 Mean absolute relative bias (%) and mean bias (%) of tracer uptake of PET-DLAC and PET-SegAC with respect to reference PET-CTAC for ^{18}F-Flutemetamol calculated for 70 brain regions

It should be noted that the training of the algorithm was performed in both 2D and 3D modes. Since 2D training mode exhibited slightly better performance, only the results associated with 2D implementation are reported in this section. Table 2 summarizes the quantitative analysis of PET-DLAC and PET-SegAC AC techniques for the entire head region reported separately for ^{18}F-Flortaucipir, ^{18}F-Flutemetamol, ^{18}F-DOPA, and ^{18}F-FDG radiotracers. The p-values calculated between DLAC and SegAC results were statistically significant ($p < .04$) for all metrics. Likewise, Table 3 presents ME, MAE and RE results for DLAC and SegAC approaches calculated within soft-tissue, air cavities, and bone regions for the four tracers. The DLAC approach resulted in improved activity recovery within both the entire head region and for each specific tissue type compared to SegAC. Except ME in soft-tissue for ^{18}F-Flutemetamol ($p = .06$), the remaining results reported in Table 2 were all statistically significant ($p < .05$). Representative coronal views of PET images corrected for attenuation using the corresponding CT images, SegAC, and DLAC approaches are shown in Figure 1 for the different radiotracers. Figures S3–S6 illustrate transaxial, coronal, and sagittal views of the patients shown in Figure 1 for ^{18}F-Flortaucipir, ^{18}F-Flutemetamol, ^{18}F-DOPA, and ^{18}F-FDG radiotracers, respectively. The corresponding difference images (PET-DLAC/PET-SegAC—PET-CTAC) are also shown beneath PET-DLAC and PET-SegAC images, which depict the voxel-wise under- and over-estimation of radiotracer uptake.

No remarkable differences were observed between the convergence of the different training folds for the entire dataset. The training and validation loss convergence of the ^{18}F-FDG dataset is shown in Figure S7. Similar trends of training and validation loss were observed for the other three radiotracers. Moreover, Table S1 summarizes the quantitative analysis of PET-DLAC and PET-SegAC AC techniques for the head region (similar to Table 2) whereas Table S2 presents the ME, MAE, and RE results for DLAC and SegAC approaches calculated within soft-tissue, air cavities, and bone regions (similar to Table 3) for the five patients belonging to the external test dataset. The evaluation
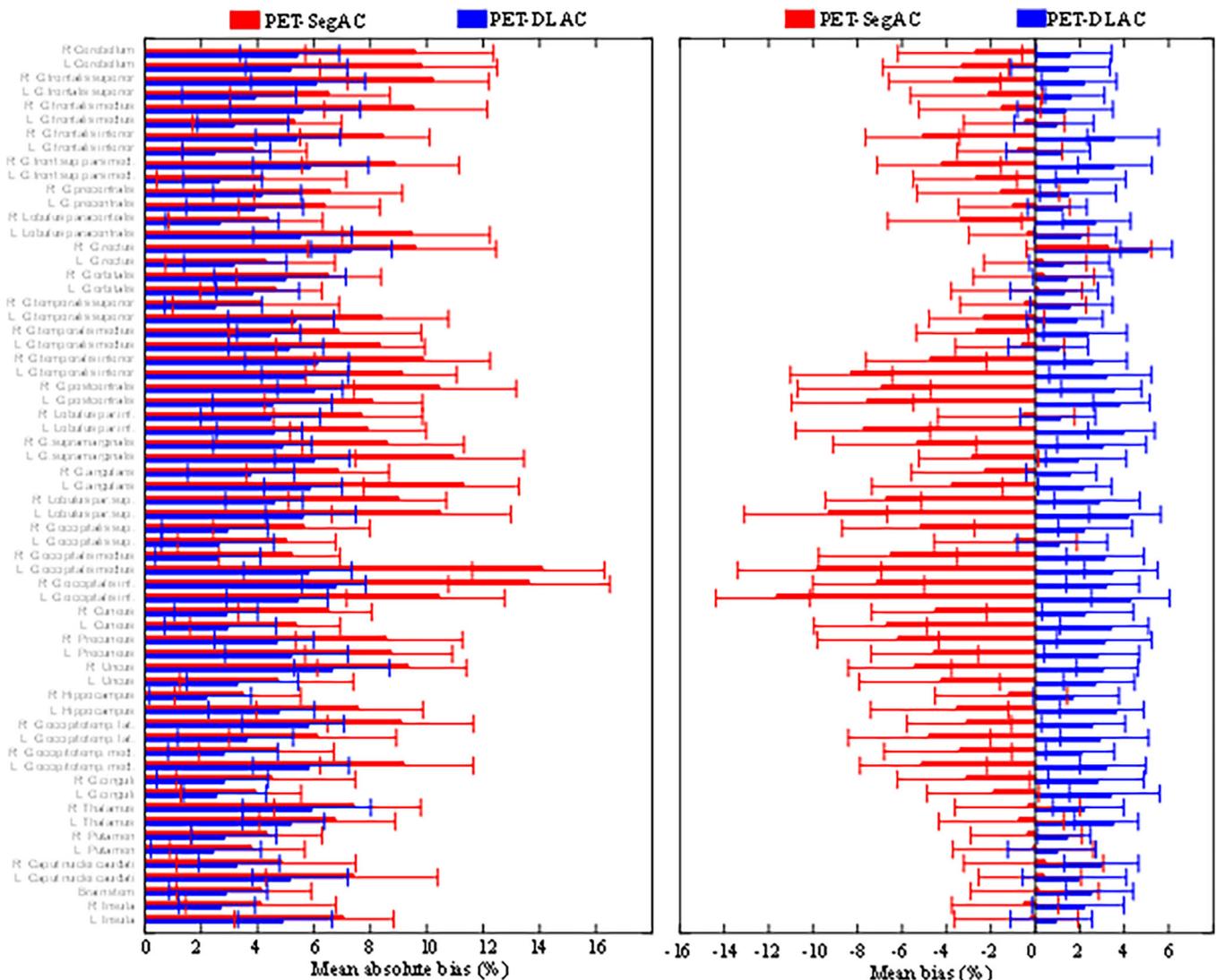
FIGURE 4 Mean absolute relative bias (%) and mean bias (%) of tracer uptake of PET-DLAC and PET-SegAC with respect to reference PET-CTAC for ^{18}F-FDG calculated for 63 brain regions

on the external test dataset did not reveal noticeable differences with respect to the results obtained from the 160 subjects of the training/validation dataset (Tables 2 and 3). In addition, consistent performance was observed across the different training folds when evaluated on the external test dataset.

The quantitative accuracy of DLAC and SegAC approaches was further assessed using region-wise analysis of PET images mapped to a common coordinate space separately for each radiotracer. Figure 2 depicts the mean relative (RE) and mean absolute relative (ARE) bias of SegAC and DLAC approaches for ^{18}F-Flortaucipir in 70 brain regions (according to MNI template) across 40 subjects. Likewise, Figure 3 depicts the RE and ARE calculated in 70 brain regions for ^{18}F-Flutemetamol. The ARE of the DLAC approach for ^{18}F-Flortaucipir and ^{18}F-Flutemetamol radiotracers barely reached 8% while SegAC led to ARE of up to 17%. The differences reported in Figures 2 and 3 between DLAC and SegAC methods were statistically significant ($p < .04$), except for Cerebellum exterior ($p = .09$), inferior temporal gyrus ($p = .08$), and medial superior frontal gyrus ($p = .08$) in Figure 2.

Similarly, Figure 4 depicts the region-wise quantitative evaluation of ^{18}F-FDG PET images for DLAC and SegAC approaches in 63 brain regions (according to the BRASS template). Slightly smaller bias was observed in ^{18}F-FDG PET images compared to ^{18}F-Flortaucipir and ^{18}F-Flutemetamol PET images. Yet, the DLAC approach led to an ARE of less than 7%, thus outperforming SegAC (ARE of up to 15%). The differences between the DLAC and SegAC approaches reported in Figure 4 were statistically significant ($p < .04$) except for the L G. orbitalis ($p = .05$).

Figure 5 presents the results of quantitative analysis of DLAC and SegAC approaches for ^{18}F-DOPA PET images within seven brain regions. In agreement with the above results, the DLAC approach outperformed SegAC, leading to less than 8% absolute quantitative bias ($p < .03$). Moreover, Figure 6 illustrates the results of the joint histogram analysis of PET-DLAC and PET-SegAC versus the reference PET-CTAC images performed over the 40 subjects for each radiotracer. The DLAC approach exhibited superior performance over SegAC resulting in significantly higher SUV correlation with the reference PET-CTAC images for all four neuroimaging radiotracers.

In addition to the quantitative evaluation, the present study focused particularly on the vulnerability of the DLAC approach to outliers. To this end, the entire dataset (containing 180 subjects) was carefully evaluated with respect to the occurrence of gross errors and outliers. We document these cases separately for each radiotracer. Figure 7 shows the single outlier observed for ^{18}F-Flortaucipir, wherein remarkable overestimation of tracer uptake is observed in the posterior region. This is the only outlier that would interfere with clinical interpretation since the other manifestations for the other radiotracers were mainly extracerebral. The intensity profiles plotted over the affected region clearly display the overestimation of tracer uptake in the PET-DLAC image compared to reference PET-CTAC and PET-SegAC images.

Figure S8 shows local SUV underestimation observed in a single ^{18}F-Flutemetamol study where the DLAC algorithm failed to recover the activity uptake within the soft-tissue region surrounded by bony structures. Two similar cases were observed in ^{18}F-FDG PET-DLAC images, one of them is shown in Figure S9, wherein the DLAC approach led to a local SUV underestimation within a region consisting of soft-tissue and bone.

Two outliers were observed in ^{18}F-DOPA PET-DLAC images where the DLAC approach Figure S10 shows one of these cases.

FIGURE 5 Mean absolute relative bias (%) and mean bias (%) of tracer uptake of PET-DLAC and PET-SegAC with respect to reference PET-CTAC for ^{18}F-DOPA calculated for seven brain regions
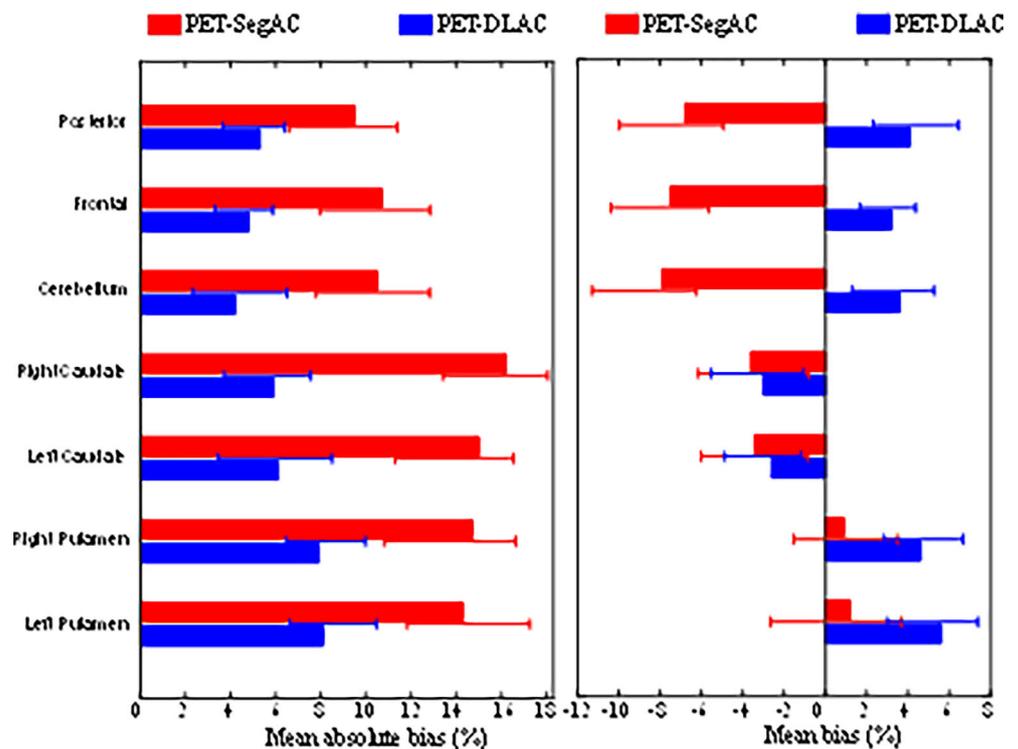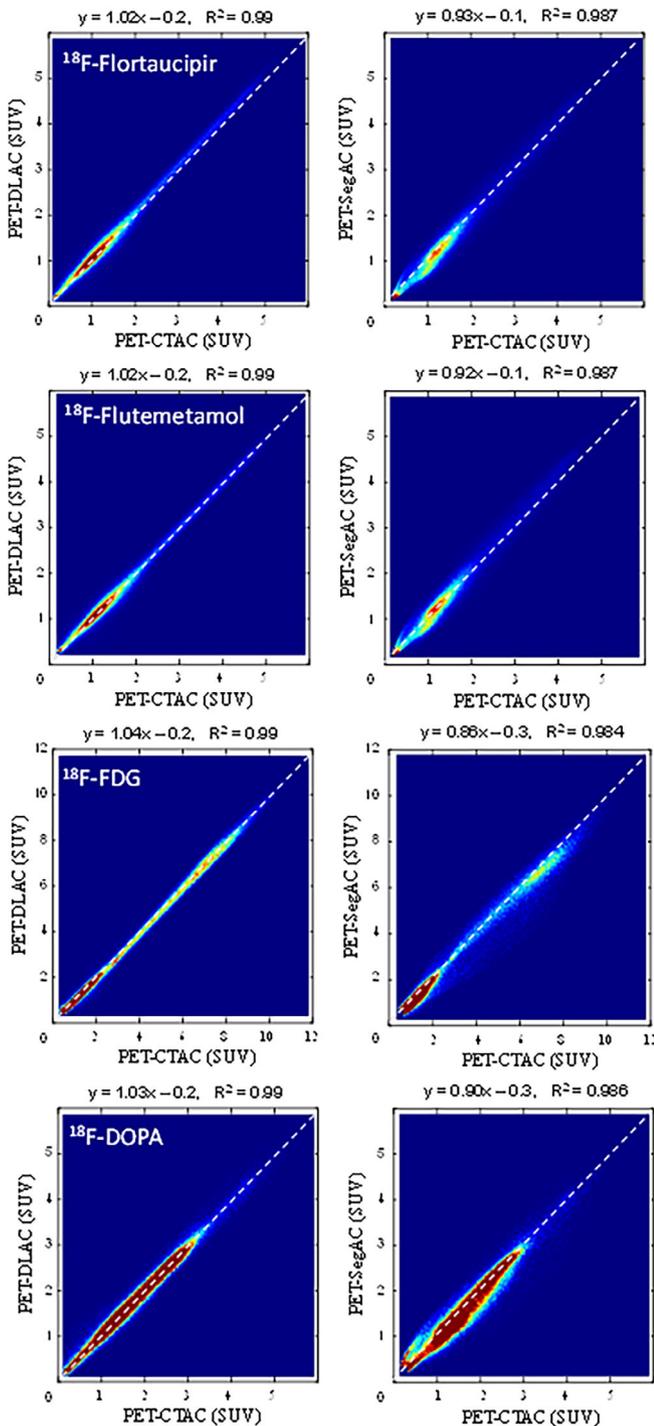
FIGURE 6 Joint histogram analysis depicting the correlation between activity concentration of PET-DLAC and PET-SegAC images versus reference PET-CTAC images for the four neuroimaging radiotracers

4 | DISCUSSION

One of the main objectives of the present work was the quantitative assessment of the joint attenuation and scatter correction of brain PET images in image-space through the use of deep learning algorithms. This approach enjoys straightforward training and data synthesis

procedure, wherein PET images corrected for attenuation and scatter are estimated in an end-to-end fashion from PET-nonAC images without the need for anatomical imaging (CT or MRI). As such, this approach is appealing and easily applicable to dedicated brain PET scanners which lack concurrent structural imaging and hybrid PET/MRI scanners.

Previous studies using this approach have shown promising results, at least when compared with other MRI-guided or CT synthesis-based AC methods (Shiri et al., 2019; Yang et al., 2019). These works focused solely on ^{18}F-FDG brain PET imaging through quantitative analysis of SUV bias and radiomic features. In the present work, we extended the evaluation of this approach to other PET neuroimaging tracers and comparison to segmentation-based technique as a bottom line for clinically relevant performance evaluation. The quantitative analysis of PET images showed reduced bias when using the DLAC approach compared to SegAC. The superior performance of the DLAC approach over SegAC was equally observed in PET images acquired with the different neuroimaging radiotracers, wherein an SUV bias of less than 8% was achieved with the DLAC approach compared to over 16% achieved by SegAC. Similar magnitude of SUV bias was observed in PET-DLAC images for all radiotracers, though a slightly smaller bias was observed in ^{18}F-FDG PET images, indicating consistent performance of this approach independent of the specific radio-tracer distribution and uptake patterns). The slightly reduced bias observed in ^{18}F-FDG PET-DLAC images was mostly due to the higher uptake of ^{18}F-FDG in the brain which rendered the relative errors less sensitive to small fluctuations. Considering the results obtained from the evaluation of ^{18}F-FDG PET images, the magnitude of SUV bias in the present study are in agreement with the two previously published works reporting on a deep learning-based algorithm for PET AC in image-space. A mean SUV bias of $-0.1 \pm 2.14\%$ (ranging from -9.5 to 10.0%) calculated over 18 patients was reported by Shiri et al. (2019) whereas a mean SUV bias of 0.2 ± 0.92 over 10 patients was reported in (Yang et al. (2019).

The quantitative evaluation of joint attenuation and scatter correction in image-space using deep learning was one of the major objectives of this work. Yet, particular attention was focused on potential susceptibility of this approach to outliers associated with the different neuroimaging radiotracers. Despite promising overall performance achieved by deep learning algorithms used in previous works, specific cases of failure leading to gross errors were reported highlighting potential clinical impact (Arabi et al., 2018; Arabi et al., 2019). In the study, conducted by Yang et al., deep learning-based AC in image-space failed in one case out of 10 subjects, where ^{18}F-FDG uptake was overestimated by about 50% (absolute SUV difference of 5) in the brain (Yang et al., 2019). In the present study, 6 outliers out of 180 subjects were observed, with four representative cases reported in Figure 7 and Supplemental Figures 8–10, in addition to 8 minor cases with similar patterns but with limited impact in terms of affected region and SUV bias. The incidence of outliers was independent of the radiotracer used as no evident connection was observed or could be established between the outliers and a specific radiotracer. Likewise, the performance of the DLAC approach was almost similar for the

FIGURE 7 Outlier report: The DLAC approach resulted in considerable pseudo-uptake in the posterior of a single ^{18}F-Flortaucipir PET study. Sagittal views of PET-CTAC, PET-SegAC, and PET-DLAC together with their corresponding SUV bias maps along with the reference CT image are presented. The plot shows SUV profiles through the three PET images
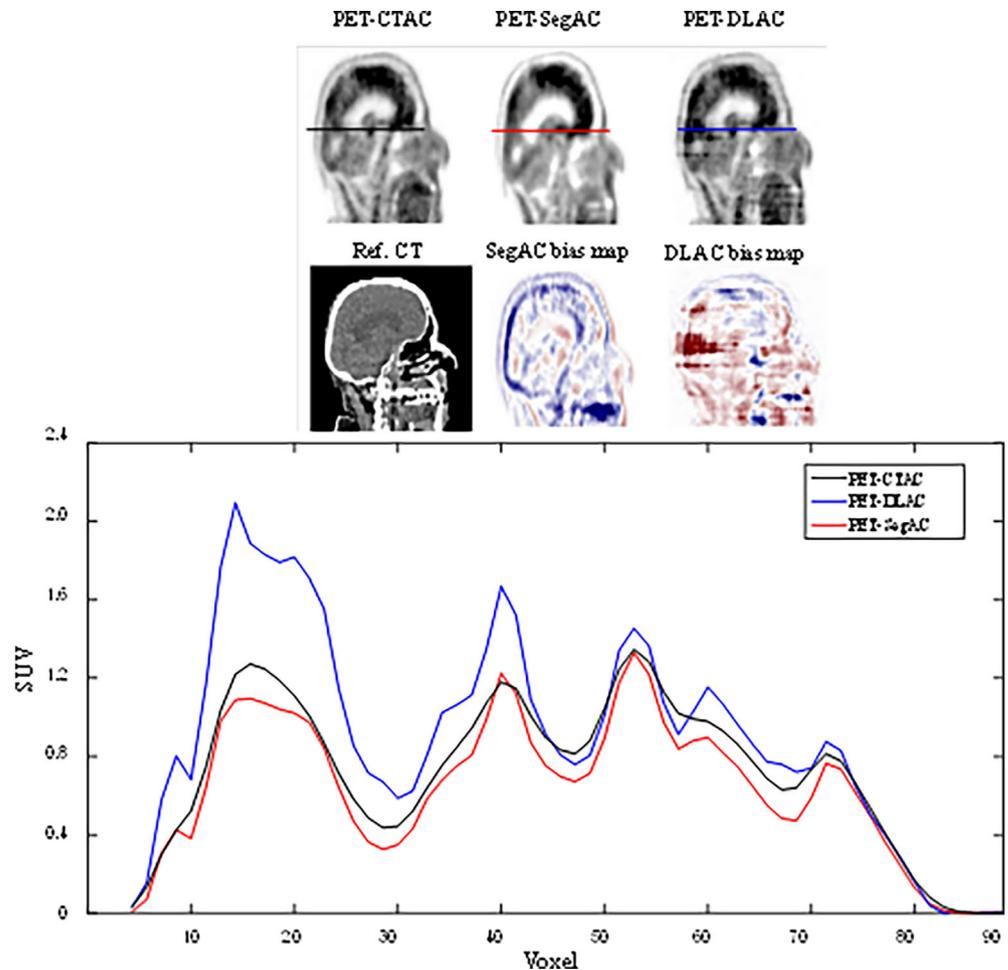
different radiotracers, wherein no specific range of bias or signal loss/distortion was observed for any radiotracers. Yet, slight differences in the quantification bias and errors were observed between the different radiotracers owing to the variable uptake patterns of the radiotracers as well as signal intensities or activity concentrations. The incidence of outliers when using deep learning-based solutions depends on the nature and complexity of the problem. In this regard, direct attenuation and scatter correction in the image domain is intrinsically an ill-posed problem, which would challenge/complicate the training of deep learning models. This is likely one of the reasons for the occurrence of outliers in this study. In this regard, an increased size of the training dataset providing a wide range of patients with a variety of anatomies/metabolisms, is a determining factor enabling machine learning algorithms to achieve higher accuracy and fewer incidence of outliers. The architecture of the network and the training procedure, such as hyperparameters setting, would also impact the incidence of outliers. Assessment of the robustness of different deep learning architectures to outliers is one of the major challenges facing the adoption of these approaches in the clinic.

The outlier reported in Figure 7 was due to technical failure of the algorithm since no peculiar anatomical variation or uptake pattern was seen in this subject. As mentioned earlier, the training of the algorithm was performed in both 2D and 3D modes. This artifact did not occur on the ^{18}F-Flortaucipir PET-DLAC images obtained from 3D

training. However, 3D training resulted in other similar types of artifacts in other patients (and in general slightly inferior quantitative accuracy); and as such, we attributed the artifact in Figure 7 to a technical failure of the deep learning approach.

The other artifacts reported in Figures S8–S10 are associated with anatomical regions wherein air or bone is adjacent to soft-tissue. In this regard, the deep learning algorithm failed to recover the actual activity concentration mostly around the center of the head region, though many regions present with even more complicated anatomical structures (such as nasal cavities with neighboring air and bone). PET-nonAC images contain weak information about anatomical structures. This challenges the deep learning algorithm to effectively recover the actual activity concentration. Inclusion of structural images, in particular MRI, would not only enhance the accuracy of this approach, but also reduce the frequency and severity of the artifacts.

PET images used in this work were acquired using a clinical PET/CT scanner following standard acquisition and reconstruction protocols adopted for each of the four radiotracers. Hence, these PET images bear virtually similar image quality and noise levels. In this light, the trained models are particularly optimized for a specific noise level and image quality. Hence, these models may perform suboptimally when input images are acquired with different noise characteristics or image quality. The models may result in larger quantitative errors and higher likelihood of outliers. This issue would be more

serious for low-dose PET imaging, wherein PET images contain high noise levels, which may lead to noise-induced outliers. To achieve satisfactory results, the training of the models should be repeated if the quality or noise levels of the input images are substantially different.

Though joint attenuation and scatter correction in image-space exhibited promising performance, special attention should be paid to potential failure of this approach, which might skew the diagnosis and clinical interpretation of the resulting PET images.

5 | CONCLUSION

Deep learning-based joint PET attenuation and scatter correction in image-space (DLAC) was quantitatively evaluated for four different PET radiotracers used in clinical neuroimaging studies. Quantitative analysis demonstrated superior performance of this approach over the segmentation-based (SegAC) method used in the clinic. The DLAC approach exhibited a very good and consistent performance regardless of the radiotracer used resulting in less than 8% absolute SUV bias compared to the SegAC method which resulted in more than 16% bias. Nevertheless, the DLAC approach is susceptible to outliers, leading to image artifacts and large quantification errors. Caution and particular attention should be paid to potential failures of the DLAC approach, which might skew the diagnosis and clinical interpretation of the resulting PET images.

CONFLICT OF INTEREST
The authors declare that they have no conflict of interest.

DATA AVAILABILITY STATEMENT
The data will be available upon request from the authors.

ORCID
Habib Zaidi https://orcid.org/0000-0001-7559-5297

REFERENCES
Arabi, H., Dowling, J. A., Burgos, N., Han, X., Greer, P. B., Koutsouvelis, N., & Zaidi, H. (2018). Comparative study of algorithms for synthetic CT generation from MRI: Consequences for MRI-guided radiation planning in the pelvic region. *Medical Physics*, *45*, 5218–5233.

Arabi, H., Koutsouvelis, N., Rouzaud, M., Miralbell, R., & Zaidi, H. (2016). Atlas-guided generation of pseudo-CT images for MRI-only and hybrid PET–MRI-guided radiotherapy treatment planning. *Physics in Medicine and Biology*, *61*, 6531–6552.

Arabi, H., Rager, O., Alem, A., Varoquaux, A., Becker, M., & Zaidi, H. (2015). Clinical assessment of MR-guided 3-class and 4-class attenuation correction in PET/MR. *Molecular Imaging and Biology*, *17*, 264–276.

Arabi, H., & Zaidi, H. (2016a). Magnetic resonance imaging-guided attenuation correction in whole-body PET/MRI using a sorted atlas approach. *Medical Image Analysis*, *31*, 1–15.

Arabi, H., & Zaidi, H. (2016b). One registration multi-atlas-based pseudo-CT generation for attenuation correction in PET/MRI. *European Journal of Nuclear Medicine and Molecular Imaging*, *43*, 2021–2035.

Arabi, H., Zeng, G., Zheng, G., & Zaidi, H. (2019). Novel adversarial semantic structure deep learning for MRI-guided attenuation correction in brain PET/MRI. *European Journal of Nuclear Medicine and Molecular Imaging*, *46*, 2746–2759.

Chiotis, K., Saint-Aubert, L., Boccardi, M., Gietl, A., Picco, A., Varrone, A., … Geneva Task Force for the Roadmap of Alzheimer's, B. (2017). Clinical validity of increased cortical uptake of amyloid ligands on PET as a biomarker for Alzheimer's disease in the context of a structured 5-phase development framework. *Neurobiology of Aging*, *52*, 214–227.

Defrise, M., Rezaei, A., & Nuyts, J. (2012). Time-of-flight PET data determine the attenuation sinogram up to a constant. *Physics in Medicine and Biology*, *57*, 885–899.

Dinkla, A. M., Wolterink, J. M., Maspero, M., Savenije, M. H. F., Verhoeff, J. J. C., Seravalli, E., … van den Berg, C. A. T. (2018). MR-only brain radiation therapy: Dosimetric evaluation of synthetic CTs generated by a dilated convolutional neural network. *International Journal of Radiation Oncology, Biology, Physics*, *102*, 801–812.

Emami, H., Dong, M., Nejad-Davarani, S. P., & Glide-Hurst, C. (2018). Generating synthetic CT s from magnetic resonance images using generative adversarial networks. *Medical Physics*, *45*, 3627–3636.

Evans, A. C., Collins, D. L., Mills, S., Brown, E., Kelly, R., & Peters, T. M., 1993. *3D Statistical Neuroanatomical Models from 305 MRI Volumes*. IEEE Conference Record Nuclear Science Symposium and Medical Imaging Conference, pp. 1813–1817.

Gibson, E., Li, W., Sudre, C., Fidon, L., Shakir, D. I., Wang, G., … Vercauteren, T. (2018). NiftyNet: A deep-learning platform for medical imaging. *Computer Methods and Programs in Biomedicine*, *158*, 113–122.

Gómez, F. J. G., Huertas, I., Ramírez, J. A. L., & Solís, D. G. (2018). Elaboración de una plantilla de SPM para la normalización de imágenes de PET con 18F-DOPA. *Imagen Diagnóstica*, *9*, 23–25.

Hammers, D. B., Atkinson, T. J., Dalley, B. C., Suhrie, K. R., Horn, K. P., Rasmussen, K. M., … Hoffman, J. M. (2017). Amyloid positivity using [18F] Flutemetamol-PET and cognitive deficits in nondemented community-dwelling older adults. *American Journal of Alzheimer's Disease and Other Dementias*, *32*, 320–328.

Han, X. (2017). MR-based synthetic CT generation using a deep convolutional neural network method. *Medical Physics*, *44*, 1408–1419.

Huynh, T., Gao, Y., Kang, J., Wang, L., Zhang, P., Lian, J., & Shen, D. (2016). Estimating CT image from MRI data using structured random forest and auto-context model. *IEEE Transactions on Medical Imaging*, *35*, 174–183.

Keereman, V., Fierens, Y., Broux, T., De Deene, Y., Lonneux, M., & Vandenberghe, S. (2010). MRI-based attenuation correction for PET/-MRI using ultrashort echo time sequences. *Journal of Nuclear Medicine*, *51*, 812–818.

Ladefoged, C. N., Law, I., Anazodo, U., Lawrence, K. S., Izquierdo-Garcia, D., Catana, C., … Hutton, B. (2017). A multi-Centre evaluation

of eleven clinically feasible brain PET/MRI attenuation correction techniques using a large cohort of patients. *NeuroImage*, *147*, 346–359.

Leuzy, A., Chiotis, K., Lemoine, L., Gillberg, P. G., Almkvist, O., Rodriguez-Vieitez, E., & Nordberg, A. (2019). Tau PET imaging in neurodegenerative tauopathies-still a challenge. *Molecular Psychiatry*, *24*, 1112–1134.

Leynes, A. P., Yang, J., Wiesinger, F., Kaushik, S. S., Shanbhag, D. D., Seo, Y., ... Larson, P. E. (2018). Zero-Echo-time and Dixon deep pseudo-CT (ZeDD CT): Direct generation of pseudo-CT images for pelvic PET/MRI attenuation correction using deep convolutional neural networks with multiparametric MRI. *Journal of Nuclear Medicine*, *59*, 852–858.

Li, W., Wang, G., Fidon, L., Ourselin, S., Cardoso, M. J., & Vercauteren, T., 2017. *On the Compactness, Efficiency, and Representation of 3D Convolutional Networks: Brain Parcellation as a Pretext Task*. International Conference on Information Processing in Medical Imaging. Springer. pp. 348–360.

Litjens, G., Kooi, T., Bejnordi, B. E., Setio, A. A. A., Ciompi, F., Ghafoorian, M., ... Sanchez, C. I. (2017). A survey on deep learning in medical image analysis. *Medical Image Analysis*, *42*, 60–88.

Liu, F., Jang, H., Kijowski, R., Bradshaw, T., & McMillan, A. B. (2017). Deep learning MR imaging–based attenuation correction for PET/MR imaging. *Radiology*, *286*, 676–684.

Liu, F., Jang, H., Kijowski, R., Zhao, G., Bradshaw, T., & McMillan, A. B. (2018). A deep learning approach for 18 F-FDG PET attenuation correction. *EJNMMI Physics*, *5*, 24.

Martinez-Moller, A., Souvatzoglou, M., Delso, G., Bundschuh, R. A., Chefd'hotel, C., Ziegler, S. I., ... Nekolla, S. G. (2009). Tissue classification as a potential approach for attenuation correction in whole-body PET/MRI: Evaluation with PET/CT data. *Journal of Nuclear Medicine*, *50*, 520–526.

Mehranian, A., Arabi, H., & Zaidi, H. (2016a). Quantitative analysis of MRI-guided attenuation correction techniques in time-of-flight brain PET/-MRI. *NeuroImage*, *130*, 123–133.

Mehranian, A., Arabi, H., & Zaidi, H. (2016b). Vision 20/20: Magnetic resonance imaging-guided attenuation correction in PET/MRI: Challenges, solutions, and opportunities. *Medical Physics*, *43*, 1130–1155.

Mehranian, A., Zaidi, H., & Reader, A. J. (2017). MR-guided joint reconstruction of activity and attenuation in brain PET-MR. *NeuroImage*, *162*, 276–288.

Melroy, S., Bauer, C., McHugh, M., Carden, G., Stolin, A., Majewski, S., ... Wuest, T. (2017). Development and design of next-generation head-mounted ambulatory microdose positron-emission tomography (AM-PET) system. *Sensors*, *17*, 1164.

Noirot, C., Mainta, I., Mendes, A., Andryszak, P., Visvaratnam, H., Unschuld, P. G., ... Garibotto, V. (2018). Tau PET imaging evidence in patients with cognitive impairment: Preparing for clinical use. *Clinical and Translational Imaging*, *6*, 471–482.

Pavese, N., & Brooks, D. J. (2009). Imaging neurodegeneration in Parkinson's disease. *Biochimica et Biophysica Acta*, *1792*, 722–729.

Shiri, I., Ghafarian, P., Geramifar, P., Leung, K. H.-Y., Ghelichoghli, M., Oveisi, M., ... Ay, M. R. (2019). Direct attenuation correction of brain PET images using only emission data via a deep convolutional encoder-decoder (Deep-DAC). *European Radiology*, *29*, 6867–6879.

Tashima, H., Yoshida, E., Inadama, N., Nishikido, F., Nakajima, Y., Wakizaka, H., ... Yamaya, T. (2016). Development of a small single-ring OpenPET prototype with a novel transformable architecture. *Physics in Medicine and Biology*, *61*, 1795–1809.

Vemuri, P., Lowe, V. J., Knopman, D. S., Senjem, M. L., Kemp, B. J., Schwarz, C. G., ... Jack, C. R., Jr. (2017). Tau-PET uptake: Regional variation in average SUVR and impact of amyloid deposition. *Alzheimer's & Dementia*, *6*, 21–30.

Wollenweber, S., Ambwani, S., Delso, G., Lonn, A., Mullick, R., Wiesinger, F., ... Fidrich, M. (2013). Evaluation of an atlas-based PET head attenuation correction using PET/CT & MR patient data. *IEEE Transactions on Nuclear Science*, *60*, 3383–3390.

Yang, J., Park, D., Gullberg, G. T., & Seo, Y. (2019). Joint correction of attenuation and scatter in image space using deep convolutional neural networks for dedicated brain (18)F-FDG PET. *Physics in Medicine and Biology*, *64*, 075019.

Zaidi, H., & Koral, K. F. (2004). Scatter modelling and compensation in emission tomography. *European Journal of Nuclear Medicine and Molecular Imaging*, *31*, 761–782.

Zaidi, H., & Montandon, M.-L. (2006). The new challenges of brain PET imaging technology. *Current Medical Imaging Reviews*, *2*, 3–13.

Zaidi, H., Montandon, M.-L., & Meikle, S. (2007). Strategies for attenuation compensation in neurological PET studies. *NeuroImage*, *34*, 518–541.

Zaidi, H., Ojha, N., Morich, M., Griesmer, J., Hu, Z., Maniawski, P., ... Shao, L. (2011). Design and performance evaluation of a whole-body ingenuity TF PET-MRI system. *Physics in Medicine and Biology*, *56*, 3091–3106.

SUPPORTING INFORMATION

Additional supporting information may be found online in the Supporting Information section at the end of this article.